A point-by-point response to the reviews

Thank you for your valuable comments. The followings are our responses to your comments.

Response to Reviewer #2

Comment 1: The idea of this manuscript is clear. In this study, the composition of particulate matter and meteorological factors were deeply explored, which provided a good guidance for the collaborative treatment of ozone and particulate matter. The manuscript not only analyzed the relationship between $PM_{2.5}$ and O_3 and the boundary layer, but also focuses on the relationship between the components of $PM_{2.5}$ and the boundary layer, which is a very valuable part of this paper. However, it has much room for improvement. The analysis of this paper is rough, many things are unclear, and key parameters are still lacking verification. The author needs to supplement relevant information. Other suggestions for improvement are listed below. To sum up, It is strongly recommended to make significant revisions to the article, otherwise it cannot be accepted.

Answer: Thank you for your approval. According to your valuable comments, we have made significant revisions to our revised manuscript.

Comment 2: Lack of data profile description. For example, how many observatories are there, and what observation elements do each station have? The author should at least add a table that fully illustrates the data.

Answer: According to your valuable suggestions, the data profile description has been added in our revised manuscript (Page 6−7, line 111−143). Our field observations were conducted based on the existing ground-level observation stations (national control station, $PM_{2.5}$ component network, etc.) in the North China Plain (NCP), which covered two megacities (BeiJ and TianJ) and 26 surrounding cities. The spatial distribution of these 28 valid sites was shown in Figure 1. Hourly concentrations of ground-level SO_2, NO_2, O_3, $PM_{2.5}$ and its chemical compositions (SO_4^{2-}, NO_3^-, NH_4^+, and OC), and meteorological variables, including air temperature, relative humidity (RH), wind speed (WS) and direction (WD), and 24-h accumulated precipitation, at the sites were obtained from the platform of National Atmospheric Particulate Chemical-Speciation-Network. This network is established to improve the understanding of the heavy pollution formation mechanism in the North China Plain (NCP) and support the decision-making of local governments and state administration. Hourly SO_2, NO_2, O_3, $PM_{2.5}$ and its chemical compositions were recorded at the $PM_{2.5}$ component network, which was selected followed the Technical Regulation for Selection of Ambient Air Quality Monitoring Station published by the Ministry of Ecology and Environment of the People's Republic of China (HJ664−2013). The monitoring sites of $PM_{2.5}$ component network were mostly set up within the cities,

and can reflect the average pollution level of each city. Details for the near-ground observation stations of $PM_{2.5}$ component network were shown in Table R1. The meteorological variables were recorded in the national meteorological observation stations, and the information of each station can be obtained from the public website of China Meteorological Administration (http://data.cma.cn/data/cdcindex/cid/0b9164954813c573.html). It should be noted that the measurement sites of meteorological variables and air pollutants were not always consistent. To better analyze the meteorological conditions for O_3 and $PM_{2.5}$, only the station closed to the air quality monitoring station and representative of the city meteorological condition was selected in our work. The temporal resolution of air temperature, RH, WS and WD was 1-h. To avoid the influence of diurnal boundary layer cycles, in this article we focused on the relationships between daily mean air pollutants and meteorological factors. The daily mean meteorological factors, $PM_{2.5}$ and its major secondary components were calculated from the hourly data; daily O_3 concentration was characterized by the maximum daily 8 h average ozone (MDA8 O_3). Details for the near-ground observation species and the metrics were shown in Table R2. It's noted that when we rechecked the observation data, it's found that the calculated maximum daily 8 h average ozone (MDA8 O_3) in the original manuscript was incorrect, and the average of daily 8 h average ozone was misused. We have corrected the value of MDA8 O_3 in the whole article and carefully checked the accuracy of all observation data in the revised manuscript.

Comment 3: Figure 2 is confusing. My understanding is that the proportion of different values occurring at a certain time should sum to 100%. But the sum expressed in the figure must be more than 100%.

Answer: We have added the calculation method of the occurrence frequency (%) mentioned in Figure 2 in the methodology (Page 7, line 144−150). To better demonstrate the overall change characteristics of regional air pollution and meteorological conditions during the observation period, the occurrence frequency (%), which means the proportion of the number of cities at each air pollutant or methodology level, was calculated based on the following equation:

$$\text{Occurrence frequency}_{X}^{level} = \frac{N_X^{level}}{\text{Total } N_X} \times 100\% \quad (1)$$

where X means the air pollutant or methodology factors, N_X^{level} represents the number of cities at each X level, $\text{Total } N_X$ represents the total number of cities. For example, as for the MLH condition, the MLHs were classified into 8 levels, and this ratio indicates the proportion of the number of cities at each MLH level to the total number of cites. As can be seen in Figure 2, on June 5, 2021, the proportion of the number of cities at MLH>2100 m was around 85 %, and significantly higher than other MLH conditions; on June 10, 2021, the MLH in all cities were lower than 1200 m, with the ratio at MLH<1200 as 100%.

Comment 4: L111 How much deviation are the two instruments for measuring the

composition of particulate matter? Were two different instruments used at different times? Please explain clearly.

Answer: MARGA (model ADI 2080) and AIM-IC (URG 9000D) have been widely utilized by government agencies and numerous research groups around the world for simultaneous measurements of water-soluble $PM_{2.5}$ constituents (Pang et al., 2021; Acharja et al., 2020; Liu et al., 2021; Liu et al., 2017; Vandenboer et al., 2014; Wang et al., 2022a; Ellis et al., 2011). They are similar in design and principle of operation. Detailed descriptions of the inlet design and the operating characteristics can be discovered in previous studies (Pang et al., 2020; Kong et al., 2018; Markovic et al., 2012; Gao et al., 2016). Previous works have shown that these two IC-based online instruments have shown good performance through instrument intercomparison studies or comparison to offline filters under clean to moderately polluted conditions (Markovic et al., 2012; Wu and Wang, 2007; Park et al., 2013; Rumsey et al., 2014). During the whole observation campaign, only one instrument (MARGA or AIM-IC) was used for ambient water-soluble $PM_{2.5}$ constituents monitoring in each station, and all instruments have been well operated to ensure the quality of observation data.

Comment 5: In view of the importance of MLH, the authors have not confirmed the calculation results. The authors use a very simple method to calculate the height of the mixed layer. It is suggested that the author make use of the meteorological profile or ERA5 reanalysis data to verify the reliability of the results.

Answer: Thank you for valuable comments. Even though the method for calculating MLH in this work seems simple, this methodology reflects the basic physical nature of the pollution mixing layer height. In recent years, many works have progressed in the atmospheric boundary layer characteristics, and analyzed the impacts of these parameter on air pollution. Planetary boundary layer (PBL), as one of the critical parameters to air quality modeling, has been well explored. However, PBL usually refers to the large-scale Ekman dynamic boundary layer (Haugen et al., 1971; Wang et al., 2014; Zhang et al., 2005). The way with which boundary layer describes the influences of air pollution is easily duplicated and confused (Niu et al., 2017). It is unreasonable to some extent, if the characteristic of the air pollution related to near-surface boundary layer is evaluated by using the concept of PBL. For air pollution measurement, one of selected functionalities of parameterization scheme for pollution mixing layer is to judge whether an air mass over a specific locality satisfies the “static and stable” attribute or not. Therefore, in this work, to express the basic physics for diagnosing meteorological conditions, we used the concept of pollution mixing layer height (MLH) proposed by (Wang et al., 2017), which was based on the classical synoptic theory according to the level of convective condensation layer, and the details of this method can be seen in previous work (Wang and Yang, 2000; Wang et al., 2017).

To be specific, we define the height close to the cloud base as the height of super-saturation layer (H_SSL), and the isoentropic atmospheric process meets the

level of convective condensation layer (LCL) in the super-saturation state, i.e., it is very close to the H_SSL. Iterative algorithm is used to work out the H_SSL (Wang and Yang, 2000):

$$H\_SSL \approx LCL = 6.11 \times 10^2 \times \left(\frac{0.622 + 0.622 \frac{e_s}{p - e_s}}{0.622 \frac{e_s}{p - e_s}} \right) \quad (2)$$

$$e_s = 6.22 \times \exp \frac{17.13(T - 273.16)}{T - 38} \quad (3)$$

where e_s represents saturated water vapor pressure, T is temperature (K). Eq. (2) can be used to calculate the H_SSL, which is favorable for pollutant mixing and represented by (P). Below this height, the atmosphere gets supersaturated, causing the pollution mixing and wetting process in the low altitude to continue, so this height is also called the height of pollution mixing layer (MLH). Thus, MLH can be derived in the following expression:

$$MLH \approx H\_SSL \approx LCL = 6.11 \times 10^2 \times \left(\frac{0.622 + 0.622 \frac{e_s}{p - e_s}}{0.622 \frac{e_s}{p - e_s}} \right) \quad (4)$$

Several works have verified the reliability of the results based on this method. With this method, Wang et al. (2017) well characterized the features of mixing layer height in highly-sensitive areas of pollution in China (1−31 December 2015 for Beijing and the same period of 1−31 December 2015 for Guangzhou), and demonstrated the schematic diagram of 3-D model for low-level super-saturation layer and pollution mixing layer in the pollution hotspots in China, such as North China Plain (NCP), Yangtze River Delta (YRD), Pearl River Delta (PRD) and Si-Chuan Basin (SCB). Wang et al. (2022b) also used this method to explore the $PM_{2.5}$ and O_3 superposition-composite pollution event during spring 2020 in Beijing, China, and the hourly evolution of MLH, O_3, and $PM_{2.5}$ during the observation period were analyzed. The results can well depict the MLH diurnal cycle, which rises at daytime and decreases at night. In addition, Niu et al. (2017) has applied this method in Beijing, and the results showed that the pollution mixing layer can well present the change characteristics of haze pollution process. In this work, we further clarified the concept of MLH, and applied this method to investigate the impacts of MLH upon the change characteristics of ozone and fine particulate matter. The above discussion has been added in our revised manuscript (Page 7−8, line 152−190).

Comment 6: Almost all the graphs in Figure 3 show the scatter distribution, why does Figure c not has a scatter plot?

Answer: According to your valuable comments, we have adjusted the presentation form of Figure 3 to better show the scatter distribution in our revised manuscript (Figure R1).

Comment 7: Generally, when the boundary layer rises, the wind speed will increase, especially when the boundary layer exceeds 1500 m, but this phenomenon is not

shown in this study. In addition, in general, when precipitation occurs, strong convection occurs, and the height of the mixing layer will suddenly rise, which is different from the author's study. Therefore, it is highly recommended that the authors validate the results of mixing layer height.

Answer: Thanks for your valuable comments. As we known, there are differences between MLH and PBLH (Height of planetary Boundary layer). These phenomena were generally summarized based on PBLH in individual cases. Besides, these phenomena can not fit each case, and there are still exceptions. According to your suggestions, we added the change characteristics of wind speed (WS) along with the increase of MLH (Figure R2 and R3). Actually, we can see apparent increase of WS when MLH in the range of 0−300 m which was probably due to precipitation events. The increase of WS when MLH exceeds 1500 have also been observed, but the increment was not so obvious. Previous works by Liu and Liang (2010) and Li et al. (2020) have found that the severe convective weather generally decreases PBLH, and the precipitation was highly negatively correlated with PBLH, which was consistent with the results found in our work. The rainfall events may produce clouds, then reduce surface solar and thermal heating, thus suppressing the PBLH. The reliability of the results based on this MLH calculation method has been verified by many works. The calculated MLHs showed strong diurnal patterns, and can well depict the change characteristics of haze pollution processes (Niu et al., 2017; Wang et al., 2022b) .

Comment 8: It is more appropriate to reflect the atmospheric oxidation capacity with the change of Ox.

Answer: The aim of Part 3.4 was to explore the superposition-composite effects and the interaction between $PM_{2.5}$ and O_3 along with the evolution of mixing layer. According to your valuable suggestions, the title of Part 3.4 has been replaced by "Superposition-composite effects of $PM_{2.5}$ and O_3 with the evolution of mixing layer". (Page 19, line 392)

Comment 9: Figure 9 can be represented as a time-by-time coloring plot, as the mean may mask the characteristics of high-altitude transport. And ozone profile results are extremely abnormal, with very little ozone decline with altitude. Ozone radar has great shortcomings in the summer when there are clouds and high humidity. Due to the extremely fast attenuation of shortwave radiation, radar echo signal will decay rapidly under the influence of water vapor, thus affecting the observation results. It is strongly suggested that delete this content.

Answer: According to your valuable suggestions, this content has been deleted in our revised manuscript. To reveal the impact of regional transport, we have presented the change characteristics of WS and WD during the typical $PM_{2.5}$-O_3 co-polluted episode.

Comment 10: The authors need to find a case to fully present the relationship between the mixing layer and pollutants, and use the hourly concentration to illustrate the response of PM, its components and ozone to the mixing layer.

Answer: According to the National Ambient Air Quality Standard of China (GB3095-2012), O_3 ($PM_{2.5}$) concentration exceeds the national air quality standard if the MDA8 O_3 (daily $PM_{2.5}$ average) concentration higher than 160 μg m^{-3} (75 μg m^{-3}). The daily $PM_{2.5}$ averages in "2+26" cities can meet the Level II national ambient air quality standard (75 μg m^{-3}), while exceeding the level I standard of 35 μg m^{-3}. Here, we defined a O_3–$PM_{2.5}$ co-polluted episode as a set of continuous days (longer than 4 days) with MDA8 O_3 and daily mean $PM_{2.5}$ in more than 10 % NCP cities exceeding 160 μg m^{-3} and 35 μg m^{-3}, respectively. According to this criterion, three typical O_3–$PM_{2.5}$ co-polluted episodes were selected: June 4–14 (Episode I), June 18–29 (Episode II), and July 2–11 (Episode III), 2021, and these three episodes have been marked in Figure 2.

According to your valuable suggestions, we find a typical $PM_{2.5}$-O_3 coordinated event (Episode II: June 18–29, 2021) during the observation period to comprehensively present the relationship between the mixing layer meteorology and air pollutants. Figure R4 and R5 showed the temporal-spatial distribution of air pollutants and meteorological factors during June 18−29, 2021. On June 18−20, MLH gradually increased from 600−1200 m to 1500−3000 m in the southern and eastern part of the NCP, $PM_{2.5}$ and MDA8 O_3 concentrations concurrently increased and showed similar spatial distributions. The wind speed dropped significantly on 20 June, and the value was lower than 1 m s^{-1} in most cities. On 21−23 June, MLH started to decrease from 1500−3000 m to 1200−1800 m, $PM_{2.5}$ and MDA8 O_3 concentrations further increased, and the areas of high $PM_{2.5}$ concentrations coincided well with those of MDA8 O_3 concentrations. During 24−25 June, MLH continued to decrease, with some values even lower than 300 m. The MLH for the areas with high MDA8 O_3 was in the range of 900−1500 m. Interestingly, the synchronized spatial change characteristics of $PM_{2.5}$ and MDA8 O_3 were consistent when MLH in the range of 900−1200 m, while inconsistent when MLH lower than 600 m. Significant rise of $PM_{2.5}$ concentration was observed in some cities with MLH lower than 300 m. It's noted that the dominant chemical composition of $PM_{2.5}$ in these areas was NO_3^-. On 28 June, the rise in MLH was observed in the central and the southern part in the NCP, and a surge of MDA8 O_3 and $PM_{2.5}$ concentrations both occurred, with 160−220 μg m^{-3} and 40−50 μg m^{-3} respectively. In general, most cities were dominated by weak winds from the east and southeast, which favored the formation of secondary pollutants from the gaseous precursors transported from the southeast part and promoted the accumulation of air pollutants.

To better understand this $PM_{2.5}$-O_3 co-polluted event, here we classified the observations during this typical event into four categories: O_3 polluted days (O_3PD; MDA8 O_3 concentration > 160 μg m^{-3} and $PM_{2.5}$ < 35 μg m^{-3}), $PM_{2.5}$ polluted days ($PM_{2.5}$PD; MDA8 O_3 concentration < 160 μg m^{-3} and $PM_{2.5}$ > 35 μg m^{-3}), O_3–$PM_{2.5}$ co-polluted days (O_3–$PM_{2.5}$CPD; MDA8 O_3 concentration > 160 μg m^{-3} and

$PM_{2.5} > 35\ \mu g\ m^{-3}$), and non-polluted days (NPD; MDA8 $O_3 < 80\ \mu g\ m^{-3}$ and $PM_{2.5} < 35\ \mu g\ m^{-3}$). Figure R6 showed the meteorological and chemical characteristic of O_3–$PM_{2.5}$ CPD, O_3 PD, $PM_{2.5}$ PD, and NPD. The results indicated that the values of MLH on O_3–$PM_{2.5}$CPD were between those on O_3PD and $PM_{2.5}$PD at around 900 m. On O_3–$PM_{2.5}$CPD, the oxidation ratio of sulfate (SOR, the molar ratio of sulfate to the sum of sulfate and SO_2) and oxidation ratio of nitrate (NOR, the molar ratio of nitrate to the sum of nitrate and NO_2) were the highest, with the values of 0.44 and 0.33, respectively, which indicated the strong secondary formation of SO_4^{2-} and NO_3^- promoted by high O_3 concentration. The $PM_{2.5}$PD occurred when MLH lower than 650 m, and the percentage of NO_3^- was the highest on $PM_{2.5}$PD. The rise of $PM_{2.5}$ in some cities under low MLH conditions may be attributed to three mechanisms. The first one is the accumulation effect due to unfavorable diffusion condition when MLH decreased. Second, these cities got little rain, and the effect of wet deposition was weak. In addition, the corresponding low T and high RH can stimulate the formation of NO_3^- from gaseous state (HNO_3). On O_3PD, the MLH was at around 1300 m, and the NOR turned to decrease, demonstrating a more significant role of partitioning process between gas and aerosol than the atmospheric oxidation process under this stage. On NPD, the MLH was the highest, with the value of about 2400 m, and the $PM_{2.5}$ chemical composition was obviously dominated by OM.

To explore the relevance of hourly O_3, $PM_{2.5}$, its components and MLH, we have taken PuY and HeZ as examples. Figure R7 plotted the day-to-day variations along with the diurnal variations of O_3, $PM_{2.5}$, its components and MLH in PuY and HeZ during Episode II (June 18−29, 2021). The results showed that there were large diurnal as well as day-to-day variability in the O_3 and $PM_{2.5}$ levels. The diurnal variations of MLH were clearly visible (Figure R8), with the rise in MLH during the daytime and the decrease in MLH at night. The concentration of $PM_{2.5}$ increased with the decrease of MLH at night, but the concentration of O_3 increased with the rise of MLH at daytime. Interestingly, we observed noontime soar of SO_4^{2-} and OC concentrations in PuY, and the values of SOR kept stable or even increased at noon. Besides, it's noted that daily O_3 and $PM_{2.5}$ both gradually accumulated with the increase of MLH during June 18−21 and 26−28, which can be attributed to the O_3 and $PM_{2.5}$ superposition composite effects. The decrease in $PM_{2.5}$ at daytime with the rise of MLH can be partly offset by an increment in secondary pollutants formation derived from O_3 growth. Then with the decrease of MLH at night, the concentration of the original existing $PM_{2.5}$ increased due to unfavorable diffusion. In general, the conclusions in this work was only suitable to the day-to-day relationship between air pollutants and MLH. The hourly relationships were more complicated and need more further analysis. According to your valuable comments, we will further explore the hourly relationship in the NCP in our follow-up studies. The above discussion has been added in our revised manuscript (Page 19−24, line 393−476).

Comment 11: As discussed in Figure 10, it is suggested that the concentration classification of MDA8 ozone can be further refined to make the change of pollutants more obvious.

Answer: According to your valuable suggestions, we have further refined the classification of MAD8 O_3 in Figure R9 (< 140 μg m^{-3}, 140–160 μg m^{-3}, 160–180 μg m^{-3}, 180–200 μg m^{-3}, > 200 μg m^{-3}). The concentrations of $PM_{2.5}$ and its major components increased synchronously with elevated MDA8 O_3 concentration, especially when MDA8 O_3 increased from < 140 to 180–200 μg m^{-3}. With elevated MDA8 O_3 concentration, SOR and NOR both slightly increased, and reached the maximum when MDA8 O_3 at around 160–200 μg m^{-3}, which indicated the strong secondary formation of SO_4^{2-} and NO_3^- promoted by high O_3 concentration. When MDA8 O_3 increased from 180–200 to > 200 μg m^{-3}, the concentrations of NO_3^-, NH_4^+, and SO_4^{2-} kept stable or started to decrease, and the values of SOR and NOR decreased synchronously. During this stage, the high O_3 concentration often accompanied with dry and hot meteorological conditions, which was not beneficial to the aqueous chemical production and was conducive to the partitioning of nitrate to the gas phase. (Page 25, line 485−498)

Comment 12: In Figure 11, it is suggested to use red for positive correlation and blue for negative correlation, with the same color scale for ozone and particulate matter. Looking at the figure, the slope of particulate matter and MLH is very low, indicating that MLH has little effect on particulate matter. Please discuss the linear p-value and R2, if there is no significant correlation, it is meaningless to discuss the rate of change alone.

Answer: Thanks to your valuable comments. We are sorry to make the mistakes about the units of $\Delta PM_{2.5}$ in Figure 11. The unit of in the original manuscript was μg m^{-3} m^{-1}, and we multiplied the values by 100 m in our revised manuscript (μg m^{-3} (100) m^{-1}). According to your valuable suggestions, we have changed and unified the color scale of for ozone and particulate matter, with red for positive correlation and blue for negative correlation in Figure R10.

Comment 13:Technical comments:
1) L221 fund? found?
2) Figure 5a and 5b It is recommended that the color of the value be uniform from small to large.

Answer: Thanks to your valuable comments. Line 211 has been rephrased (Page 14) and the color of the values in Figure 5a and 5b have been uniformed from small to large in our revised manuscript (Figure R11 and R12).

References

Acharja, P., Ali, K., Trivedi, D. K., Safai, P. D., Ghude, S., Prabhakaran, T., and Rajeevan, M.: Characterization of atmospheric trace gases and water soluble inorganic chemical ions of PM_1 and $PM_{2.5}$ at Indira Gandhi International Airport, New Delhi during 2017–18 winter, Sci. Total Environ., 729, 138800, https://doi.org/10.1016/j.scitotenv.2020.138800, 2020.

Ellis, R. A., Murphy, J. G., Markovic, M. Z., VandenBoer, T. C., Makar, P. A., Brook, J., and Mihele, C.: The influence of gas-particle partitioning and surface-atmosphere exchange on ammonia during BAQS-Met, Atmos. Chem. Phys., 11, 133-145, 10.5194/acp-11-133-2011, 2011.

Gao, J., Peng, X., Chen, G., Xu, J., Shi, G.-L., Zhang, Y.-C., and Feng, Y.-C.: Insights into the chemical characterization and sources of $PM_{2.5}$ in Beijing at a 1-h time resolution, Sci. Total Environ., 542, 162-171, https://doi.org/10.1016/j.scitotenv.2015.10.082, 2016.

Haugen, D. A., Kaimal, J. C., Bradley, E. F.: An experimental study of Reynolds stress and heat flux in the atmospheric surface layer, Q. J. Roy. Meteor. Soc., 97, 168-180, 1971.

Kong, L., Du, C., Zhanzakova, A., Cheng, T., and Zhang, S.: Trends in heterogeneous aqueous reaction in continuous haze episodes in suburban Shanghai: An in-depth case study, Sci. Total Environ., 634, 1192, 10.1016/j.scitotenv.2018.04.086, 2018.

Li, Y., Zhang, H., Zhang, Q., Zhang, A., Yang, J., Zhang, C.: Response characteristics of atmospheric boundary layer height to summer monsoon activity and monsoon precipitation of monsoon swing region in the eastern part of northwest China, Arid Land Geography, 2020, 43,1169-1178

Liu, J., Wu, D., Fan, S., Mao, X., and Chen, H.: A one-year, on-line, multi-site observational study on water-soluble inorganic ions in $PM_{2.5}$ over the Pearl River Delta region, China, Sci. Total Environ., 601-602, 1720-1732, 10.1016/j.scitotenv.2017.06.039, 2017.

Liu, S. and Liang, X.: Observed diurnal cycle climatology of planetary boundary layer height, J. Clim., 23, 5790-5809, 2010.

Liu, Y., Feng, Z., Zheng, F., Bao, X., Liu, P., Ge, Y., Zhao, Y., Jiang, T., Liao, Y., Zhang, Y., Fan, X., Yan, C., Chu, B., Wang, Y., Du, W., Cai, J., Bianchi, F., Petäjä, T., Mu, Y., He, H., and Kulmala, M.: Ammonium nitrate promotes sulfate formation through uptake kinetic regime, Atmos. Chem. Phys., 21, 13269-13286, 10.5194/acp-21-13269-2021, 2021.

Markovic, M. Z., VandenBoer, T. C., and Murphy, J. G.: Characterization and optimization of an online system for the simultaneous measurement of atmospheric water-soluble constituents in the gas and particle phases, J. Environ. Monit., 14, 1872-1884, 10.1039/c2em00004k, 2012.

Niu, T., Wang, J., Yang, Y., Wang, Y., and Chen, C.: A study on parameterization of the Beijing winter heavy haze events associated with height of pollution mixing layer, Adv. Meteorol., 2017, 1-11, 10.1155/2017/8971236, 2017.

Pang, N., Gao, J., Zhu, G., Hui, L., Zhao, P., Xu, Z., Tang, W., and Chai, F.: Impact of clean air action on the $PM_{2.5}$ pollution in Beijing, China: Insights gained from two

heating seasons measurements, Chemosphere, 263, 127991, 10.1016/j.chemosphere.2020.127991, 2021.
Pang, N., Gao, J., Che, F., Ma, T., Liu, S., Yang, Y., Zhao, P., Yuan, J., Liu, J., Xu, Z., and Chai, F.: Cause of $PM_{2.5}$ pollution during the 2016-2017 heating season in Beijing, Tianjin, and Langfang, China, J. Environ. Sci. (China), 95, 201-209, 10.1016/j.jes.2020.03.024, 2020.
Park, S. S., Jung, S. A., Gong, B. J., Cho, S. Y., and Lee, S. J.: Characteristics of $PM_{2.5}$ haze episodes revealed by highly time-resolved measurements at an air pollution monitoring supersite in Korea, Aerosol Air Qual. Res., 13, 957-976, 10.4209/aaqr.2012.07.0184, 2013.
Rumsey, I. C., Cowen, K. A., Walker, J. T., Kelly, T. J., Hanft, E. A., Mishoe, K., Rogers, C., Proost, R., Beachley, G. M., Lear, G., Frelink, T., and Otjes, R. P.: An assessment of the performance of the Monitor for AeRosols and GAses in ambient air (MARGA): a semi-continuous method for soluble compounds, Atmos. Chem. Phys., 14, 5639-5658, 10.5194/acp-14-5639-2014, 2014.
VandenBoer, T. C., Markovic, M. Z., Sanders, J. E., Ren, X., Pusede, S. E., Browne, E. C., Cohen, R. C., Zhang, L., Thomas, J., Brune, W. H., and Murphy, J. G.: Evidence for a nitrous acid (HONO) reservoir at the ground surface in Bakersfield, CA, during CalNex 2010, J. Geophys. Res. Atmos., 119, 9093-9106, 10.1002/2013jd020971, 2014.
Wang, J., Yang, Y.: Modern weather engineering. Meteorological Press, Beijing, 334–339, 2000.
Wang, J., Bian, L., Xiao, C.: Dynamics of ekman boundary layer over the antarctic plateau in summer, Chinese Sci. Bull., 59, 999–1005, 2014.
Wang, J., Yang, Y., Zhang, X., Liu, H., Che, H., Shen, X., and Wang, Y.: On the influence of atmospheric super-saturation layer on China's heavy haze-fog events, Atmos. Environ., 171, 261-271, 10.1016/j.atmosenv.2017.10.034, 2017.
Wang, J., Gao, J., Che, F., Wang, Y., Lin, P., and Zhang, Y.: Dramatic changes in aerosol composition during the 2016-2020 heating seasons in Beijing-Tianjin-Hebei region and its surrounding areas: The role of primary pollutants and secondary aerosol formation, Sci. Total Environ., 849, 157621, 10.1016/j.scitotenv.2022.157621, 2022a.
Wang, J., Yang, Y., Jiang, X., Wang, D., Zhong, J., and Wang, Y.: Observational study of the $PM_{2.5}$ and O_3 superposition-composite pollution event during spring 2020 in Beijing associated with the water vapor conveyor belt in the northern hemisphere, Atmos. Environ., 272, 10.1016/j.atmosenv.2022.118966, 2022b.
Wu, W. and Wang, T.: On the performance of a semi-continuous $PM_{2.5}$ sulphate and nitrate instrument under high loadings of particulate and sulphur dioxide, Atmos. Environ., 41, 5442-5451, https://doi.org/10.1016/j.atmosenv.2007.02.025, 2007.
Zhang, G., Bian, L., Wang, J., Yang, Y., Yao, W., Xu, X.: The boundary layer characteristics in the heavy fog formation process over Beijing and its adjacent areas, Sci. China Earth Sci., 48, 88–101, 2005.
Zhao, W., Tang, G., Yu, H., Yang, Y., Wang, Y., Wang, L., An, J., Gao, W., Hu, B., Cheng, M., An, X., Li, X., and Wang, Y.: Evolution of boundary layer ozone in

Shijiazhuang, a suburban site on the North China Plain, J. Environ. Sci. (China), 83, 152-160, 10.1016/j.jes.2019.02.016, 2019.

Table R1. List of observation stations and locations.

No.	Site	Abbreviation	Station	longitude (°E)	latitude (°N)
1	BeiJing	BeiJ	China National Environmental Monitoring Centre	116.41	40.04
2	Tianjin	TianJ	Zhongshan North Road Station	117.21	39.17
3	Shijiazhuang	SJZ	Northwest Shuiyuan Station	114.49	38.13
4	Langfang	LangF	Langfang Hebei University of Technology Station	116.70	39.55
5	Baoding	BaoD	Yangguang North Street Station	115.48	38.93
6	Tangshan	TangS	Xiaoshan Station	118.19	39.62
7	Handan	HanD	Guangming South Street Station	114.50	36.57
8	Hengshui	HengS	Hengshui Ecology and Environment Bureau Station	115.68	37.73
9	Xingtai	XingT	Quanbei Street Station	114.53	37.09
10	Cangzhou	CangZ	Cangzhou Technical College Station	116.82	38.28
11	Taiyuan	TaiY	Taiyuan Jinyuan Station	112.48	37.71
12	Yangquan	YangQ	Nanzhuang Road Station	113.59	37.85
13	Changzhi	ChangZ	Changzhi Ecology and Environment Bureau Station	113.11	36.20
14	Jincheng	JinC	Jincheng Ecology and Environment Bureau Station	112.86	35.49
15	Jinan	JiNan	Jinan Environmental Monitoring Station	117.06	36.66
16	Zibo	ZiB	Beijing Road station	117.91	36.84
17	Jining	JiNing	Jinyu Road Station	116.63	35.43
18	Dezhou	DeZ	Baima Lake Station	115.83	36.95
19	Liaocheng	LiaoC	Liaocheng monitoring center Station	115.98	36.50
20	Binzhou	BinZ	Binzhou Ecology and Environment Bureau Station	118.01	37.38
21	Heze	HeZ	Heze Quality Supervision	115.53	35.21

			Bureau Station		
22	Zhengzhou	ZhengZ	Zhengzhou Forty-seven Middle School Station	113.74	34.77
23	Kaifeng	KaiF	Jinming West Street Station	114.30	34.80
24	Anyang	AnY	Anyang Ecology and Environment Bureau Station	114.40	36.09
25	Hebi	HeB	Hebi Ecology and Environment Bureau Station	114.29	35.72
26	Xinxiang	XinX	Xinxiang Ecology and Environment Bureau Station	113.92	35.30
27	Jiaozuo	JiaoZ	Fengshou Middle Road Station	113.28	35.21
28	Puyang	PuY	Jinti Road Station	115.04	35.76

Table R2. List of observation species and metrics.

Species	Unit	Temporal resolution	Metrics
Gaseous pollutants			
O_3	μg m^{-3}	1 h	Maximum daily 8 h average
SO_2	μg m^{-3}	1 h	Daily average
NO_2	μg m^{-3}	1 h	Daily average
$PM_{2.5}$ and its major components			
$PM_{2.5}$	μg m^{-3}	1 h	Daily average
SO_4^{2-}/ NO_3^-/ NH_4^+	μg m^{-3}	1 h	Daily average
OC	μg m^{-3}	1 h	Daily average
Meteorological variables			
Temperature (T)	°C	1 h	Daily average
Relative Humidity (RH)	%	1 h	Daily average
Wind speed (WS)	m s^{-1}	1 h	Daily average
Wind direction (WD)	°	1 h	Daily average
24-h precipitation	mm	24 h	24-h accumulated

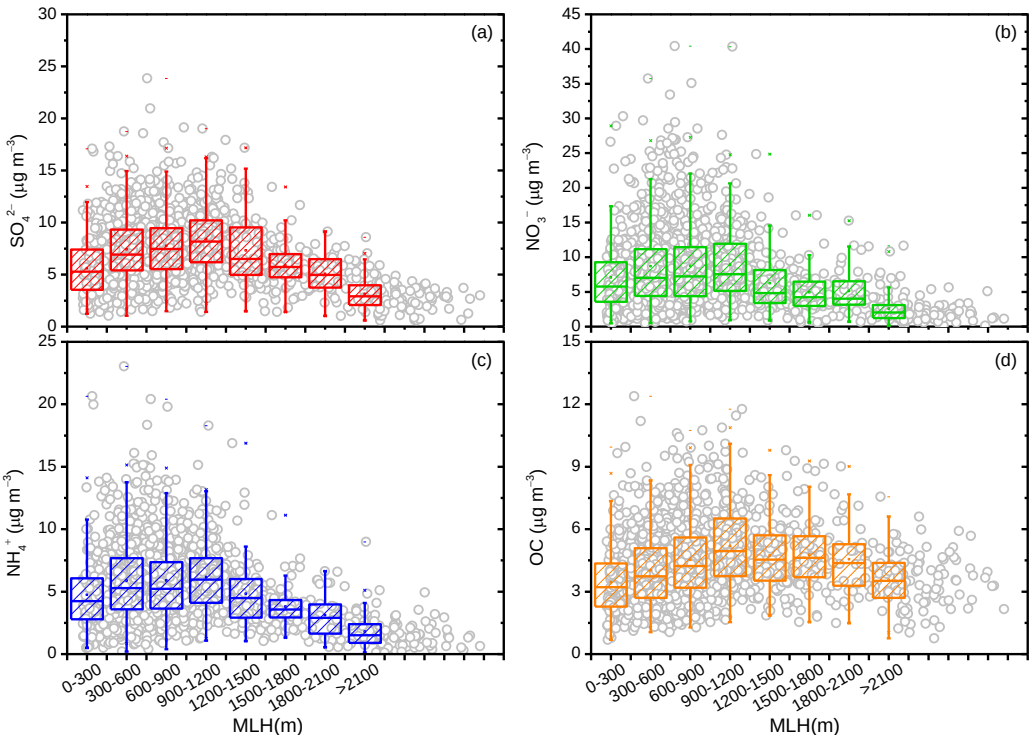

Figure R1. The variation characteristics of (a) SO_4^{2-}, (b) NO_3^-, (c) NH_4^+, and (d) OC in different MLH conditions. Box plots show the inter quartile range (the distance between the bottom and the top of the box), median (the band inside the box), and 95 % confidence interval (whiskers above and below the box) of the data.

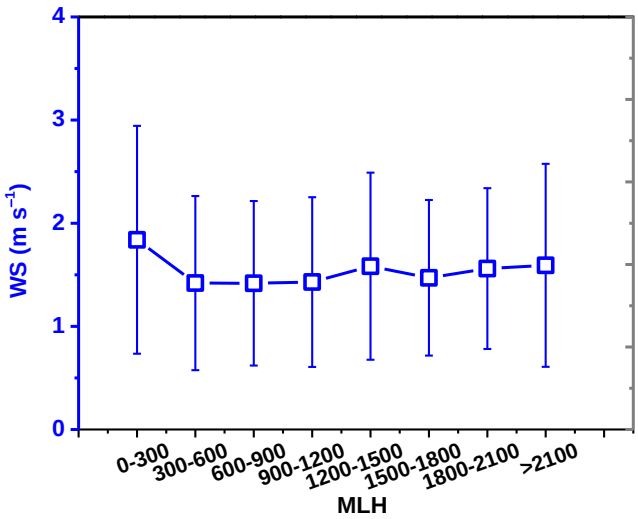

Figure R2. The change characteristics of WS under different MLH conditions.

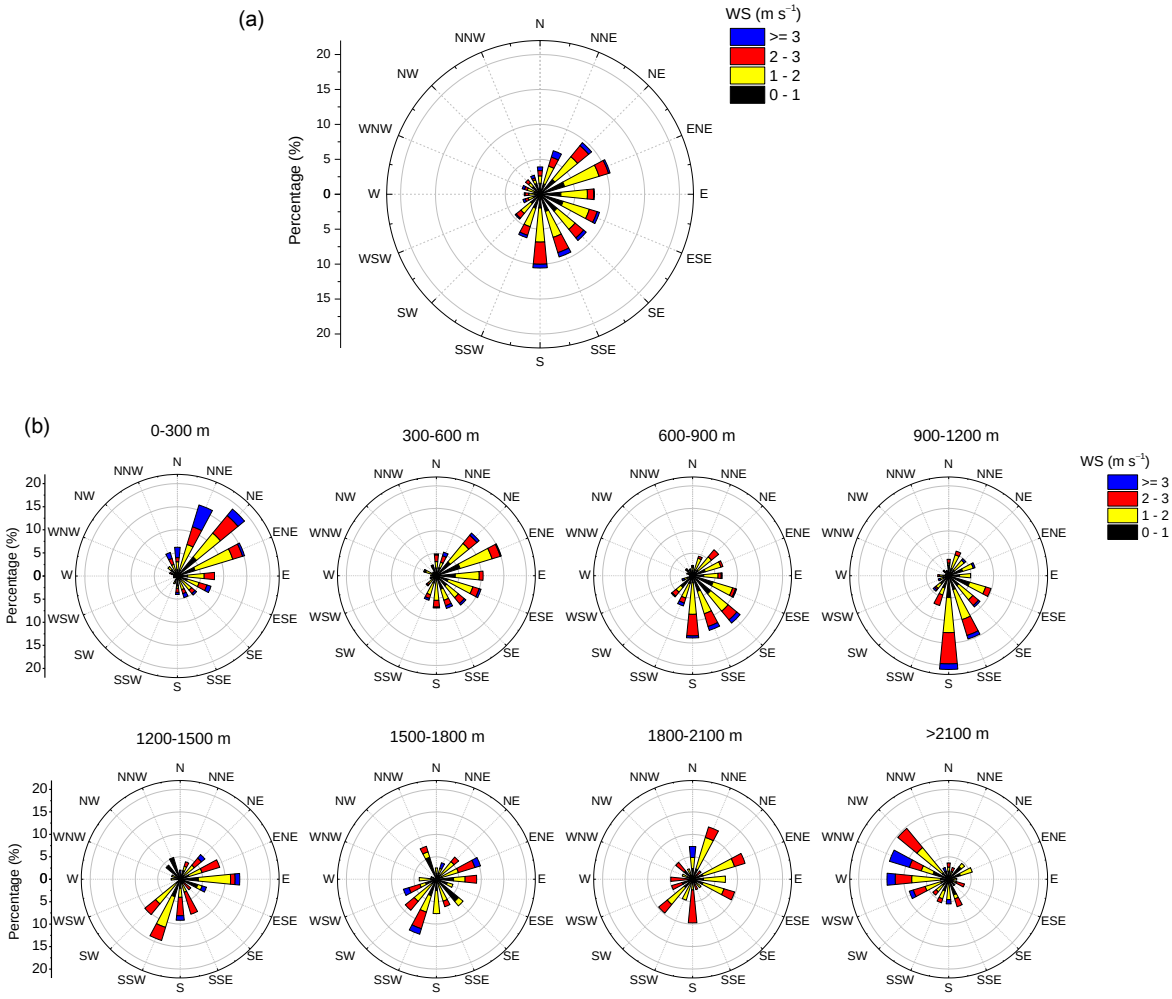

Figure R3. (a) The overall WS and WD condition during the observation campaign, (b) the change characteristics of WS and WD under different MLH levels. S: south; N: north; E: east; W: west.

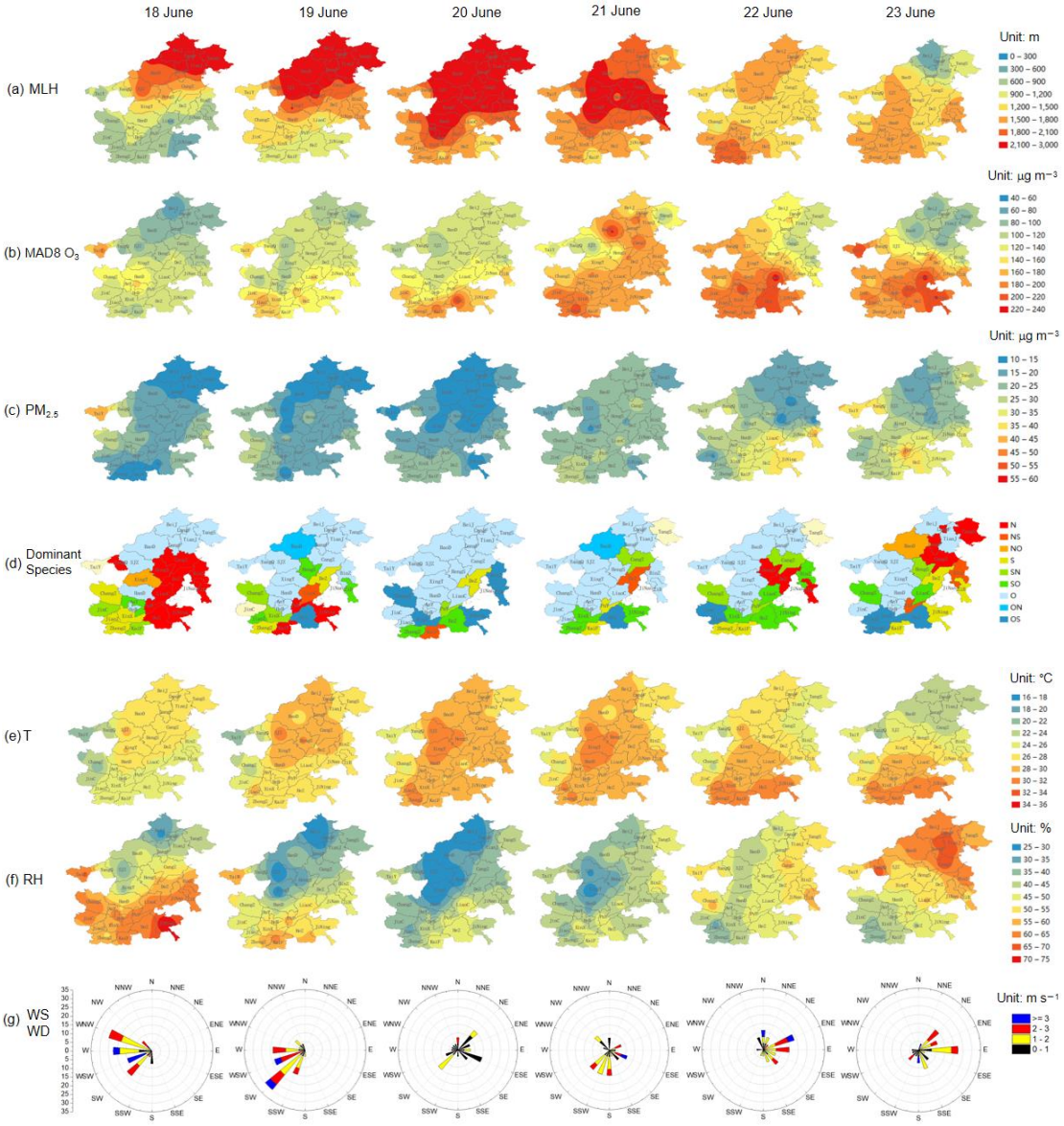

Figure R4. The spatial distribution of (a) MLH, (b) MDA8 O_3, (c) $PM_{2.5}$, (d) the dominant $PM_{2.5}$ chemical component (N: NO_3^- dominant, NS: NO_3^- and SO_4^{2-} dominant, NO: NO_3^- and OM dominant, S: SO_4^{2-} dominant, SN: SO_4^{2-} and NO_3^- dominant, SO: SO_4^{2-} and OM dominant, O: OM dominant, ON: OM and NO_3^- dominant, OS: OM and SO_4^{2-} dominant), (e) T, and (f) RH, (g) the overall change characteristics of WS and WD in the NCP from June 18 to 23, 2021.

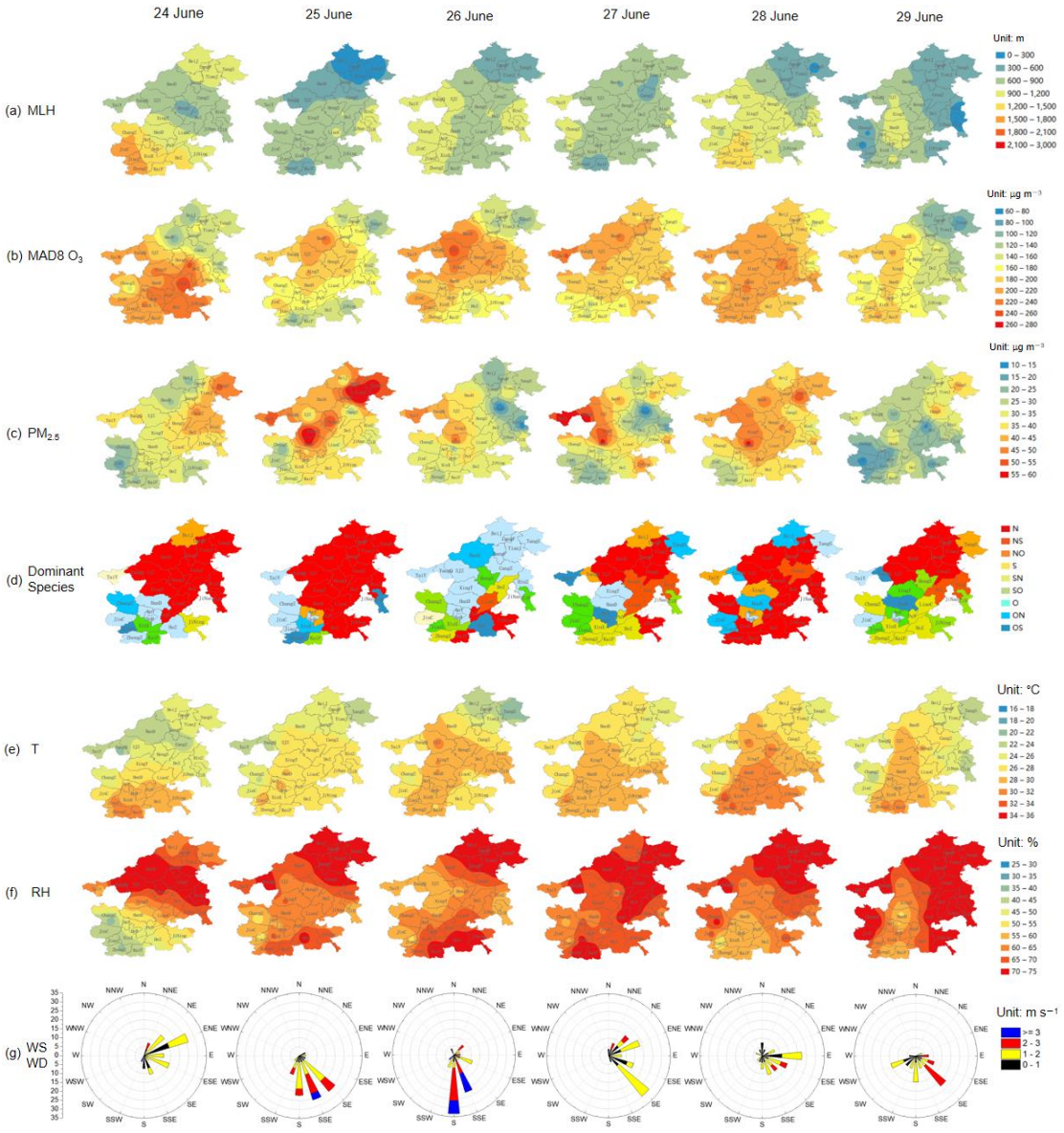

Figure R5. The spatial distribution of (a) MLH, (b) MDA8 O_3, (c) $PM_{2.5}$, (d) the dominant $PM_{2.5}$ chemical component (N: NO_3^- dominant, NS: NO_3^- and SO_4^{2-} dominant, NO: NO_3^- and OM dominant, S: SO_4^{2-} dominant, SN: SO_4^{2-} and NO_3^- dominant, SO: SO_4^{2-} and OM dominant, O: OM dominant, ON: OM and NO_3^- dominant, OS: OM and SO_4^{2-} dominant), (e) T, and (f) RH, (g) the overall change characteristics of WS and WD in the NCP from June 24 to 29, 2021.

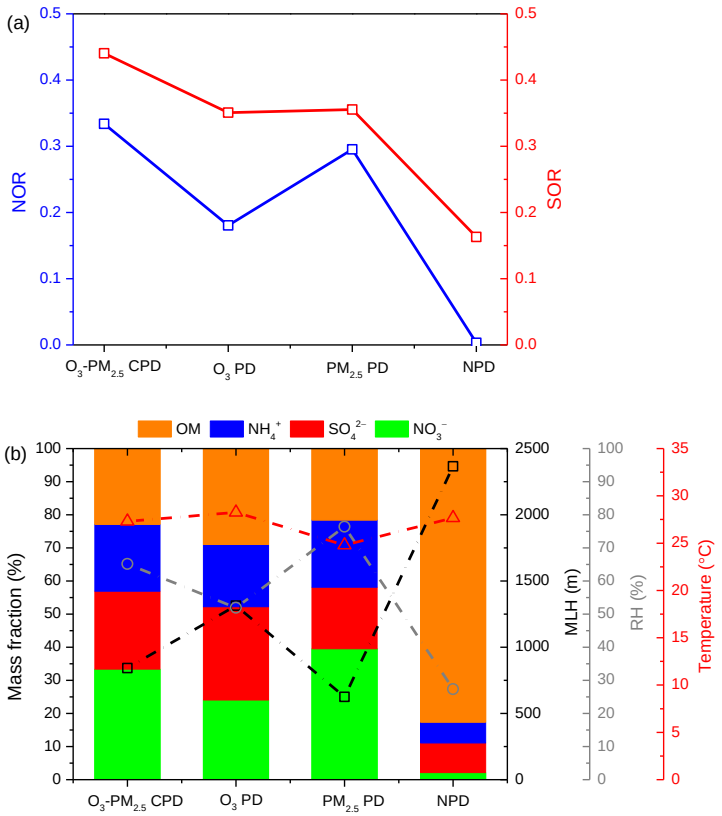

Figure R6. The distribution characteristics of (a) NOR and SOR, and (b) the mass fractions of major $PM_{2.5}$ components, MLH, RH, and T under O_3–$PM_{2.5}$ CPD, O_3 PD, $PM_{2.5}$ PD, and NPD conditions from June 24 to 29, 2021.

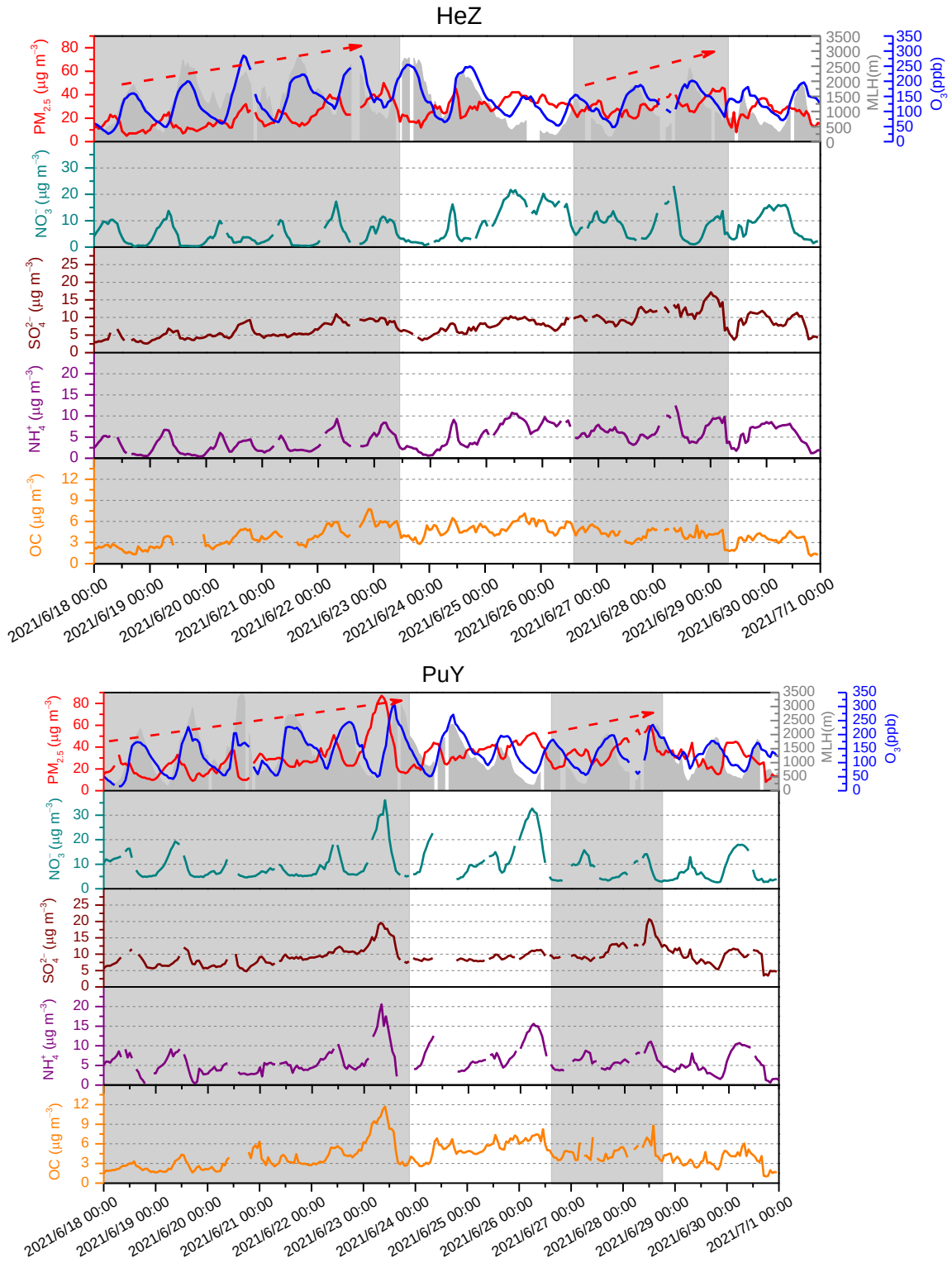

Figure R7. The hourly evolution of O_3, $PM_{2.5}$, its components and MLH in HeZ and PuY during June 18−29, 2021.

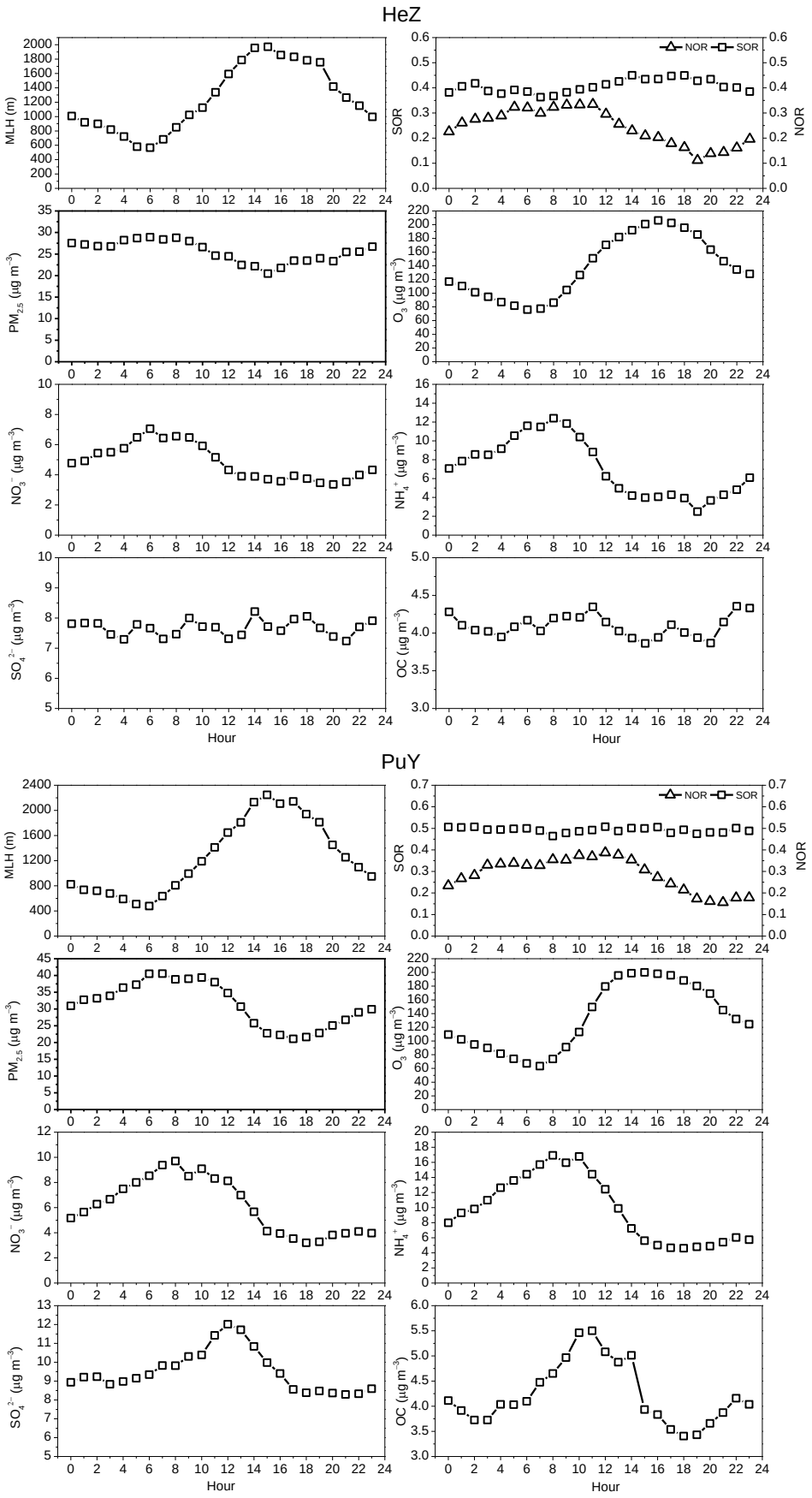

Figure R8. The diurnal variation of MLH, SOR, NOR, O_3, $PM_{2.5}$, and its components in HeZ and PuY during June 18−29, 2021.

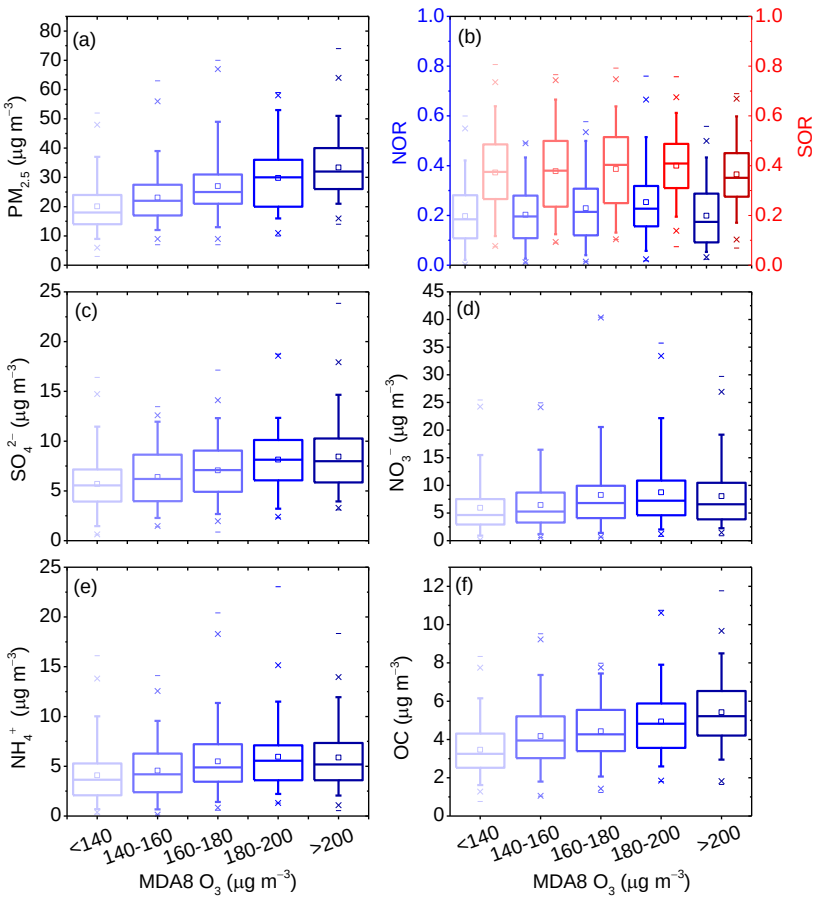

Figure R9. Box plots showing the statistics of (a) $PM_{2.5}$, (b) NOR and SOR, (c) SO_4^{2-}, (d) NO_3^-, (e) NH_4^+, and (f) OC for different MDA8 O_3 conditions (< 140 μg m^{-3}, 140–160 μg m^{-3}, 160–180 μg m^{-3}, 180–200 μg m^{-3}, > 200 μg m^{-3}). The distance between the bottom and the top of the box reflects the inter quartile range; the line and square in between are the median and mean values, respectively. The whiskers above and below the box refer the 95 % confidence interval of the data. Note that rainy days were excluded.

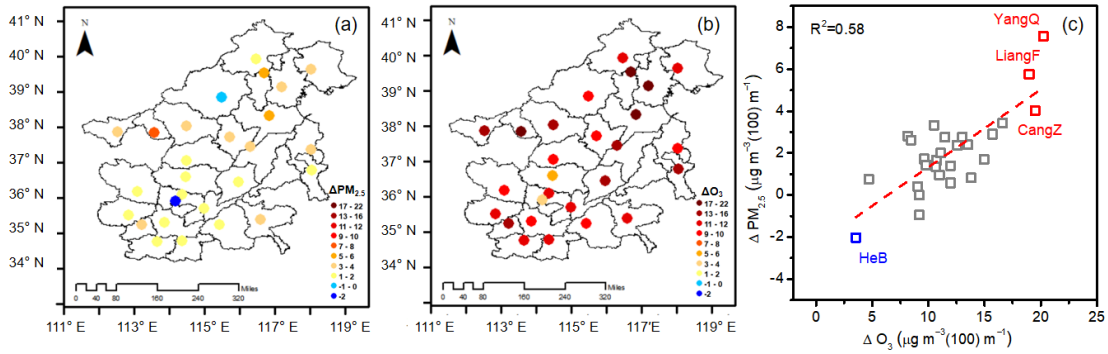

Figure R10. The spatial distribution of (a) $\Delta PM_{2.5}$ and (b) ΔO_3. (c) The relationships between $\Delta PM_{2.5}$ and ΔO_3 in the NCP during summertime. The corresponding correlation coefficients (R^2) was given at the top of the panel.

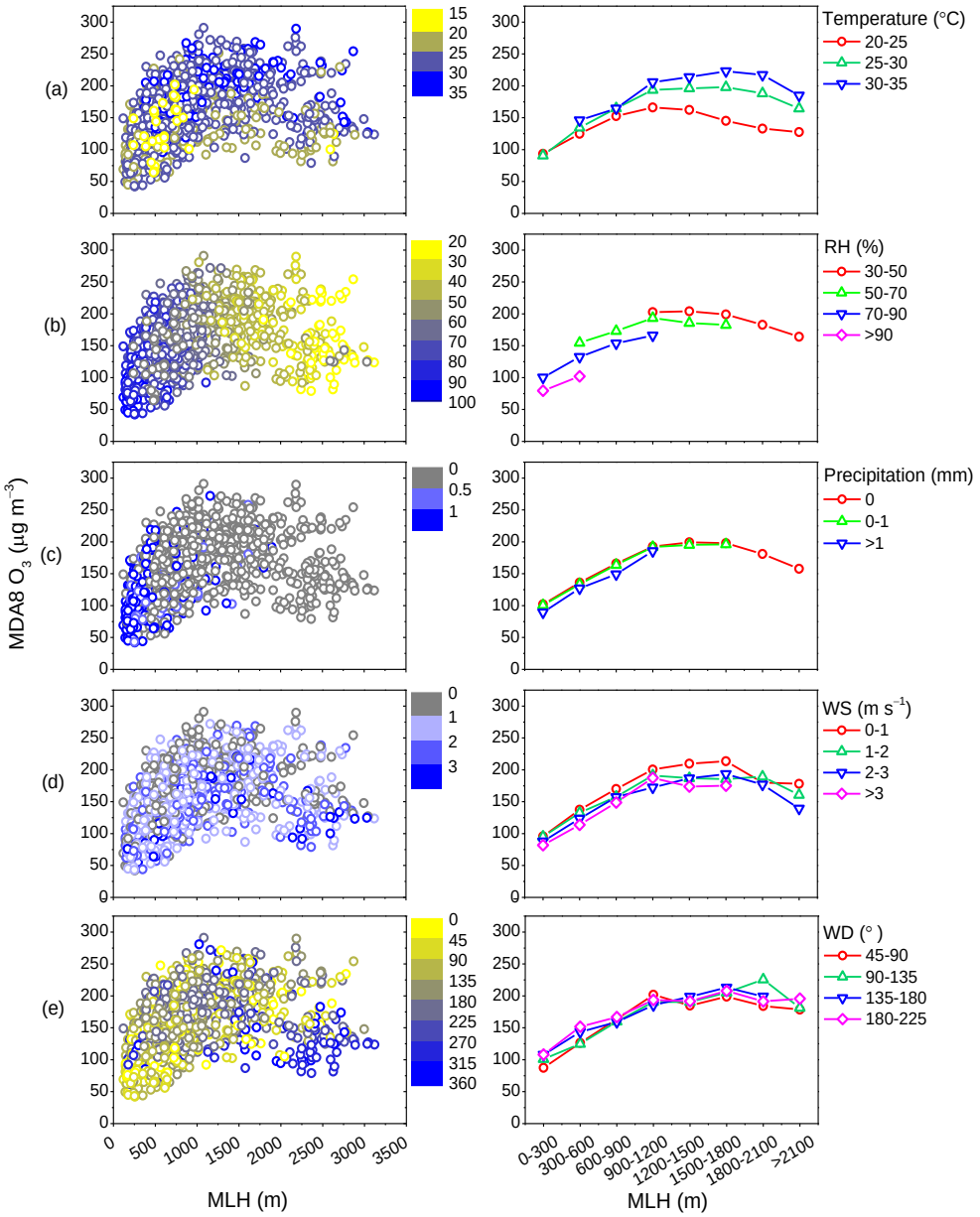

Figure R11. The distribution characteristics of the MDA8 O_3 concentrations with the evolution of MLH under different (a) temperature, (b) RH, (c) precipitation, (d) WS, and (e) WD conditions.

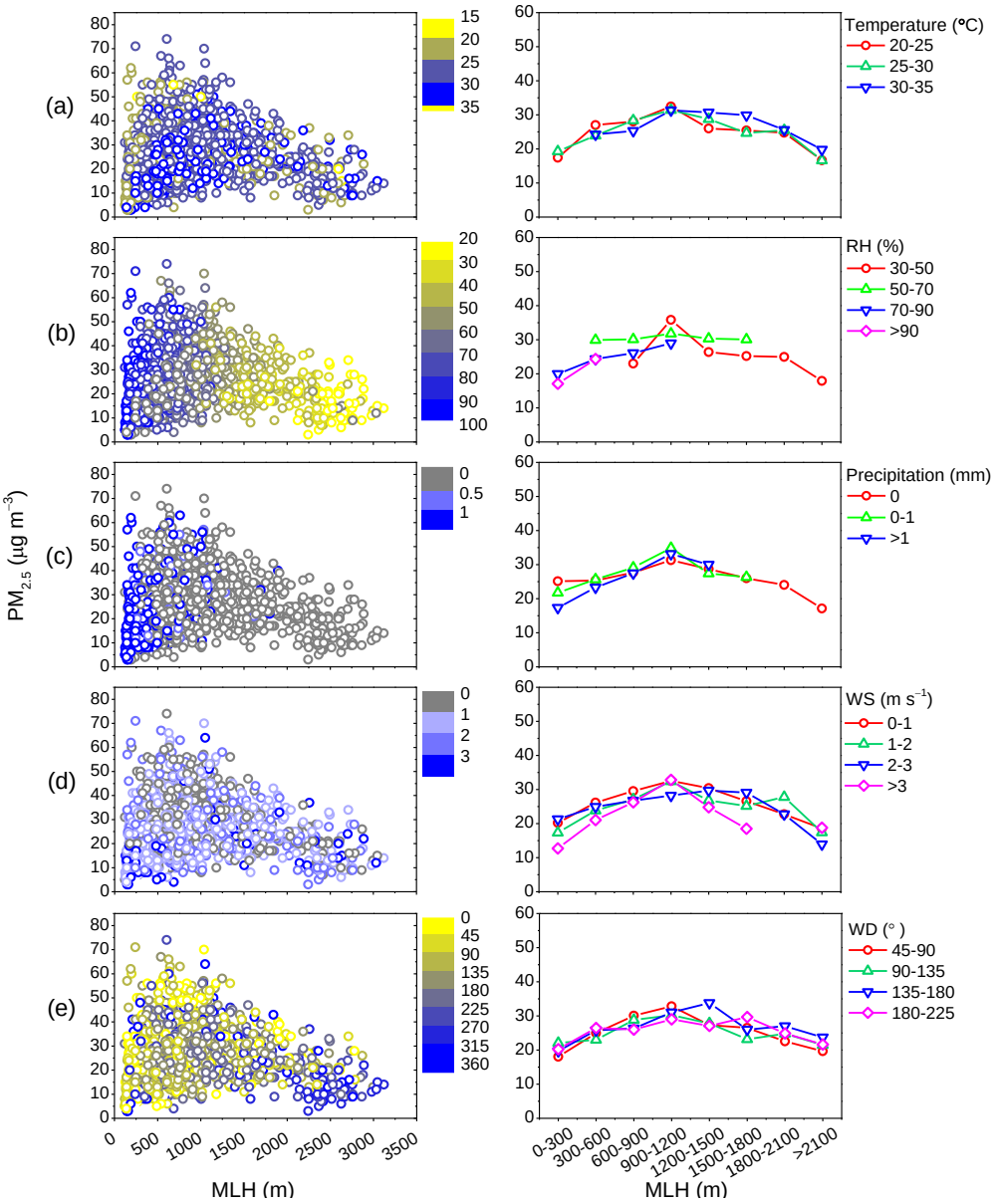

Figure R12. The distribution characteristics of the $PM_{2.5}$ concentrations with the evolution of MLH under different (a) temperature, (b) RH, (c) precipitation, (d) WS, and (e) WD conditions.